Available online at www.sciencedirect.com
ScienceDirect
International Journal of Heat and Mass Transfer 51 (2008) 3656–3668
International Journal of HEAT and MASS TRANSFER
www.elsevier.com/locate/ijhmt

Large-eddy simulation of transition to turbulence in natural convection in a horizontal annular cavity

E.L.M. Padilla, A. Silveira-Neto *

Federal University of Uberlândia, School of Mechanical Engineering, Uberlândia-MG 38408-902, Brazil

Received 29 September 2006; received in revised form 5 January 2007
Available online 11 April 2008

Abstract

Large-eddy simulations (LES) of transition to turbulence in a horizontal annular cavity are performed, using a dynamic sub-grid scale model and second order schemes for time and space discretizations. Solutions for Prandtl number of 0.707 and Rayleigh number up to 7.5×10^5 are obtained. The onset of transition to turbulence and turbulence regimes are pointed out, as well as the dynamic characteristics of the thermal plume transition. The instantaneous and time average behavior of the flows, related to the velocity and temperature fields, are analyzed and compared with numerical and experimental results from other authors. The influence of transitional and turbulent flows on local and mean Nusselt number are also investigated.

Keywords: Natural convection; Transition to turbulence; Dynamic model

1. Introduction

The natural convection problem in horizontal annular cylindrical cavities has been the subject of research over the last seven decades. This is due to the numerous technological applications in several engineering areas (nuclear, aeronautics, solar, mechanics and others). In this section, we present a brief review of selected experimental and numerical papers which allows to know the advances in transition to turbulence and turbulence research.

One of the first investigations, Beckmann [1], considered an annular cavity between concentric cylinders in the horizontal position filled with air, hydrogen and carbon dioxide. Several values of radii ratio (η) were considered in order to analyze their influence on the overall heat transfer coefficient. Later, other investigations [2–4] were done in order to study the effect of different parameters on the local and overall heat transfer coefficient for several kinds of fluids. New experimental techniques allowed to obtain important informations concerning to stable and unstable flows [5–9]. Kuenh and Goldstein [7] studied natural convection in annular cavities filled with pressurized nitrogen over a Rayleigh number range of $2.2 \times 10^2 \leqslant Ra \leqslant 7.7 \times 10^7$ and for $\eta = 2.6$. The results showed that the flow is unstable in the plume region for $Ra = 2 \times 10^5$ and that the flow becomes turbulent as Ra is increased. Also, they reported that over the inner cylinder the flow is turbulent and that under the inner cylinder the flow is laminar. McLeod and Bishop [8] studied this problem using helium at cryogenic temperatures for $8 \times 10^6 \leqslant Ra \leqslant 2 \times 10^9$ and for expansion number 0.25–1.0. They have presented sketches that show the oscillating thermal plume for $Ra = 1 \times 10^7$ and the dramatic changes of this structure as Ra is increased up to 10^9. Labonia and Guj [9] have performed experiments to analyze oscillatory and transitional flows for $0.90 \times 10^5 \leqslant Ra \leqslant 3.37 \times 10^5$ and for $\eta = 2.36$, using air at atmospheric pressure. It was verified that the mechanisms of transition to chaos have been differentiated by different dynamical indicators. Most of the referred authors have presented correlations to calculate the heat transfer coefficient. A new correlation is presented by Itoh et al.

* Corresponding author. Tel.: +55 34 32394149; fax: +55 34 32394282.
E-mail address: aristeus@mecanica.ufu.br (A. Silveira-Neto).

0017-9310/$ - see front matter © 2007 Elsevier Ltd. All rights reserved.
doi:10.1016/j.ijheatmasstransfer.2007.07.025

[10], which is based on the redefinition of the characteristic length.

Analytical solutions were one of the first method used to analyze natural convection. Expansion in series, perturbation method and boundary layer theory were also used. Since the work of Crawford and Lemlich [11], that used the interactive method of Gauss Seidel, numerical methods have been considered as an interesting and very promising tool of analysis and investigation of laminar [12–16] and turbulent [17–19,23,25] flows. Results for two-dimensional simulations using k–ε model (considering symmetry in the vertical plane) were presented by Farouk and Guçeri [17], Kenjeres and Hanjalic [19] and Char and Hsu [18]. Three-dimensional analysis of laminar flows were performed by Fusegi and Farouk [20] and Vafai and Ettefagh [21,22]. After, Desai and Vafai [23] used a wall function approach coupled with the standard k–ε model to analyze flows for $1 \times 10^6 \leqslant Ra \leqslant 1 \times 10^9$ and for several values of Pr (Prandtl number) and η. Information about the unstable nature of the turbulent natural convection are presented in [24,25]. Fukuda et al. [24] employed direct numerical simulation for Ra up to 6×10^5, $Pr = 0.71$, $\eta = 2.0$ and aspect ratio $\lambda = 2.8$. The results of flow's oscillations in transition to turbulence and some characteristic of thermal plume were presented. Miki et al. [25] used the LES technique with the Smagorinsky sub-grid scale model for $2.5 \times 10^6 \leqslant Ra \leqslant 1.18 \times 10^9$ and for several values of Pr, η, λ and the Smagorinsky constant. The effects of these parameters on turbulent properties were pointed out.

The above-mentioned works have contributed significatively to understand of natural convection problem in horizontal annuli. Moreover, the regime of transition to turbulence has been not extensively studied. On the other hand, the study of transition to turbulence requires a well resolved direct numerical simulation, but, for the majority of the problems, it is not yet possible due the actual computational resources. In this context, in the present work the authors look for to contribute to this challenging problem using LES methodology with dynamic sub-grid scale model.

2. Physical problem

The physical problem, analyzed in the present work, is the flow generated by natural convection in a horizontal annular cavity, filled with air. The fluid properties are: the kinematic viscosity ν, the thermal diffusivity α, the thermal expansion coefficient β, and the thermal conductivity, κ. The domain of analysis is bounded by two concentric cylinders with isothermal surfaces of axial length L_a, as shown in Fig. 1. The radii of the inner and outer cylinders are R_i and R_o and the surface temperature are T_i and T_o, respectively, for the inner and outer cylinders, where $T_i > T_o$. The width of the gap $L = R_o - R_i$ and the dimensionless parameters radii ratio $\eta = R_o/R_i$ and the aspect ratio $\lambda = L_a/L$ were defined. Additionally, two other

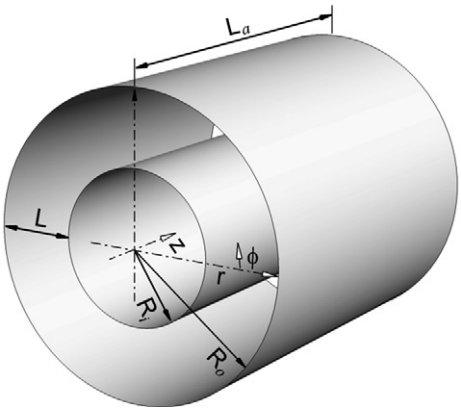

Fig. 1. Sketch of the physical configuration.

dimensionless parameters were defined, the Rayleigh and the Prandtl numbers:

$$Ra = \frac{g\beta(T_i - T_o)L^3}{\nu\alpha}, \quad Pr = \frac{\nu}{\alpha}, \tag{1}$$

where g is the acceleration of gravity.

3. Mathematical model

The mathematical formulation, for the described physical problem, is based on the fundamental laws for transport phenomena, resulting in mass conservation, Navier–Stokes and energy equations. The fluid is considered as incompressible and Newtonian with constant physical proprieties, except for the buoyancy force which is modeled via the Boussinesq approximation. The density variation is caused by fluid's thermal expansion, and it is given by $\rho = \rho_o(1 - \beta(T_i - T_o))$ with $\beta = -(1/\rho_o)(\partial\rho/\partial T)_p$, where ρ_o is the density at a reference temperature. The resulting dimensionless equations are obtained using the length scale L, the velocity scale ν/L, the pressure scale $\rho_o\nu^2/L^2$, the temperature scale $(T_i - T_o)$ and the time scale L^2/ν. So, the mass conservation, the momentum and the energy equations are given by

$$\frac{\partial u_i}{\partial x_i} = 0, \tag{2}$$

$$\frac{\partial u_i}{\partial t} + \frac{\partial(u_i u_j)}{\partial x_j} = -\frac{1}{\rho_o}\frac{\partial p}{\partial x_i} - \frac{Ra}{Pr}Tg_i + \frac{\partial}{\partial x_j}\left[\frac{\partial u_i}{\partial x_j} + \frac{\partial u_j}{\partial x_i}\right], \tag{3}$$

$$\frac{\partial T}{\partial t} + \frac{\partial(u_j T)}{\partial x_j} = \frac{\partial}{\partial x_j}\left[\frac{1}{Pr}\frac{\partial T}{\partial x_j}\right], \tag{4}$$

where u_i are the velocity components, p is the pressure, T is the temperature and $Gr = Ra/Pr$ is the Grashof number. The directions of g_i components are $(-\sin\phi, -\cos\phi, 0)$, where ϕ is angular direction (Fig. 1).

The no-slip and the impermeability boundary conditions are imposed at the cylinder surfaces, as well as the temperature. In the axial and angular directions the periodic boundary condition is applied for all variables.

3.1. Turbulence model

The LES methodology [26] consider the decomposition of flow variables, e.g. u_i, into a large scale component ($\bar{u}_i$) and a sub-grid scale (u'_i) component using a filtering process [27]. It requires the use of a filter function $G(x,x')$, which is, for the present work, a simple local grid average. So, the filtered velocity is defined by

$$\bar{u}_i(x) = \int u_i(x')G(x,x')\mathrm{d}x'. \tag{5}$$

The filtering process applied to the Navier–Stokes equations and to the energy conservation equation provide similar equations like (2)–(4). When the advective terms $\partial(\overline{u_iu_j})/\partial x_j$ and $\partial(\overline{u_jT})/\partial x_j$ are decomposed, one obtains the global sub-grid tensor and the global heat flux [28] defined as $\tau_{ij} = -(\overline{u_iu_j} - \bar{u}_i\bar{u}_j)$ and $q_j = -(\overline{u_jT} - \bar{u}_j\overline{T})$.

Considering that the sub-grid scales are more homogeneous and isotropic and also less affected by boundary conditions, the sub-grid Reynolds stress tensor and the sub-grid heat flux, are modeled using the Boussinesq hypothesis. As presented in [26,29] these sub-grid tensor and sub-grid flux may be given by

$$\tau_{ij} = -2\nu_t\overline{S}_{ij} + \frac{2}{3}k\delta_{ij}, \tag{6}$$

$$q_j = -\alpha_t\frac{\partial\overline{T}}{\partial x_j}, \tag{7}$$

where, ν_t, α_t, k and δ_{ij} are the turbulent viscosity, the turbulent diffusivity, the turbulent kinetic energy and the Kronecker delta, respectively. The strain rate tensor is defined as:

$$\overline{S}_{ij} = \frac{1}{2}\left(\frac{\partial\bar{u}_i}{\partial x_j} + \frac{\partial\bar{u}_j}{\partial x_i}\right). \tag{8}$$

Incorporating the Eqs. (6) and (7) to the filtered Navier–Stokes equations and adding the turbulent kinetic energy to the pressure term, the turbulence equations are given by

$$\frac{\partial\bar{u}_i}{\partial x_i} = 0, \tag{9}$$

$$\frac{\partial\bar{u}_i}{\partial t} + \frac{\partial(\bar{u}_i\bar{u}_j)}{\partial x_j} = -\frac{\partial\bar{p}}{\partial x_i} - \frac{Ra}{Pr}\overline{T}g_i + \frac{\partial}{\partial x_j}\left[\nu_{ef}\left(\frac{\partial\bar{u}_i}{\partial x_j} + \frac{\partial\bar{u}_j}{\partial x_i}\right)\right], \tag{10}$$

$$\frac{\partial\overline{T}}{\partial t} + \frac{\partial(\bar{u}_j\overline{T})}{\partial x_j} = \frac{\partial}{\partial x_j}\left[\alpha_{ef}\frac{\partial\overline{T}}{\partial x_j}\right], \tag{11}$$

with

$$\nu_{ef} = 1 + \nu_t, \quad \alpha_{ef} = \frac{1}{Pr} + \frac{\nu_t}{Pr_t}. \tag{12}$$

Several values of the turbulent Prandtl number (Pr_t) have been used to solve turbulent flows with heat transfer, e.g. Eidson [29] has used $Pr_t = 0.4$ and Yoshizawa [30] and Miki et al. [25] have used 0.83. In the present work, $Pr_t = 0.6$ was used as in Silveira-Neto et al. [31]. The ν_t is calculated using the dynamic sub-grid scale model [32,33].

3.2. Dynamic sub-grid scale model

The dynamic sub-grid scale model, proposed by Germano [32], represents an important advance over the Smagorinsky model [26] due to the fact that Smagorinsky constant was replaced by a dynamic function $C(\vec{x},t)$, evaluated during the simulation. This procedure eliminates some problems like the use of an ad-hoc constant in the use of a sub-grid model for transitional flows, turbulent rotational flows and for flows near walls.

The Germano [32] model is based on an algebraic identity between the sub-grid Reynolds stress tensor and the resolved turbulent tensors for two level of the filtering process. The second filter, called the test filter, is performed using the small resolved scales. Hence, the relation developed for $C(\vec{x},t)$ by Germano [32] and modified by Lilly [33] is expressed as:

$$C(\vec{x},t) = -\frac{1}{2}\frac{L_{ij}M_{ij}}{M_{ij}M_{ij}}. \tag{13}$$

The Leonard tensor L_{ij} and the tensor M_{ij} are defined by

$$L_{ij} = \widehat{\bar{u}_i\bar{u}_j} - \widehat{\bar{u}}_i\widehat{\bar{u}}_j, \tag{14}$$

$$M_{ij} = \widehat{\overline{\Delta}}^2|\widehat{\overline{S}}|\widehat{\overline{S}}_{ij} - \overline{\Delta}^2\widehat{|\overline{S}|\overline{S}_{ij}}, \tag{15}$$

where operator ($\widehat{\ }$) represents the test filtering process. The characteristic grid filter width is $\overline{\Delta} = (\prod_{i=1}^{3}\Delta_i)^{1/3}$ (Δ_i is the grid step in the i direction), the characteristic test filter width is $\widehat{\overline{\Delta}} = 2\overline{\Delta}$ [32,33] and the magnitude of the strain rate tensor is given by $|\widehat{\overline{S}}| = (2\widehat{\overline{S}}_{ij}\widehat{\overline{S}}_{ij})^{1/2}$. The test filter is a box filter, applied by a three-point weighed averaging in i direction.

By assuming that the sub-grid scales are in local equilibrium, for which a balance holds between the sub-grid scale turbulent production and turbulent dissipation rate, the ν_t can be derived as:

$$\nu_t = C(\vec{x},t)\overline{\Delta}^2|\overline{S}|. \tag{16}$$

Eq. (13) can present negative values of $C(\vec{x},t)$, resulting in negative ν_t, that is interpreted as the modeling for the back-scattering energy transfer process [32,34,35]. Unfortunately, negative values of $C(\vec{x},t)$ lead to numerical instability. Therefore, the criterion $C(\vec{x},t) = \max[0.0, C(\vec{x},t)]$ was used [36,37].

4. Numerical method

The governing equations were discretized using the finite volume method [38,39] on a staggered grid. The second order time discretization of Adams–Brashforth and the second order central difference scheme were employed. The pressure–velocity coupling was performed by the fractional-step [40]. Eq. (10) is fractioned in two steps called predictor and corrector, defined by the following equations:

$$\frac{\widetilde{\bar{u}}_i - \bar{u}_i^t}{\Delta t} = \frac{3}{2}F(\bar{u}_i)^t - \frac{1}{2}F(\bar{u}_i)^{t-1} - \left[\frac{\partial \bar{p}}{\partial x_i}\right]^t, \quad (17)$$

$$\frac{\bar{u}_i^{t+1} - \widetilde{\bar{u}}_i}{\Delta t} = -\frac{\partial p'}{\partial x_i}, \quad (18)$$

where $\widetilde{\bar{u}}_i$ is the estimated velocity. The term $F(\bar{u}_i)$ incorporates the advective, the diffusive and the buoyancy terms. The application of the divergence of Eq. (18) leads to a Poisson equation for the pressure correction p', i.e:

$$\frac{\partial^2 p'}{\partial x_i \partial x_i} = \frac{1}{\Delta t}\left[\frac{\partial \widetilde{\bar{u}}_i}{\partial x_i}\right]. \quad (19)$$

The solution procedure used is: Eq. (17) is first solved for $\widetilde{\bar{u}}_i$, p' is calculated from Eq. (19), Eq. (18) is solved for correct $\bar{u}$ at time step $(t+1)$ and finally, the pressure is corrected by $\bar{p}^{t+1} = \bar{p}^t + p'$. The Poisson equation is solved with the strongly implicit procedure (SIP) [41].

Usually, refined grid and small time step are required in LES [42], where the time step depends basically on the *Re* and on the grid dimension. In order to have stability, the CFL (Courant–Friedrichs–Lewy) stability criterion was used [43] with CFL = 0.25. A non-uniform grid was employed in the radial direction (r) and an uniform grid was employed in the angular (ϕ) and axial (z) directions. The grid was refined near the walls with an expansion/reduction factor $F = 1.05$ in accordance with:

$$\Delta r = a(F^{i-1}), \quad a = \frac{1-F}{1-F^{M/2}}\left[\frac{L}{2}\right], \quad (20)$$

where Δr is the grid spacing, M is the grid resolution in r direction and $1 \leqslant i \leqslant M/2$.

5. Results and discussion

5.1. Stable flow

Simulations were performed for $10^2 \leqslant Ra \leqslant 10^5$, with $\eta = 2$ and 2.6 and $\lambda = 1$. A grid of $20 \times 80 \times 2$ in r, ϕ, z directions (two-dimensional approximation) was used. The *Ra* range was selected based on experimental results [14,44], that show that the annular cavity flow become unstable for $Ra \cong 10^5$. Previously, the grid independency of solutions has been tested for $Ra = 4.7 \times 10^4$ and $\eta = 2.6$ with different grids. The variation in the mean Nusselt number obtained by $20 \times 80 \times 2$ and $24 \times 90 \times 2$ grids is 0.33%.

The results obtained for $Ra = 10^2$–10^4 showed a standard flow, similar to the numerical results of [6,7,17,16]. For $Ra = 10^2$ the transport process is dominated basically by diffusion and for $Ra = 10^4$ the advective transport process predominates and the thermal plume appears in the upper part of the cavity. When *Ra* is increased up to 10^5 a symmetrical but finer plume is obtained. Qualitative and quantative comparisons were performed with numerical and experimental results of Kuenh and Goldstein [6] and are present in Figs. 2 and 3.

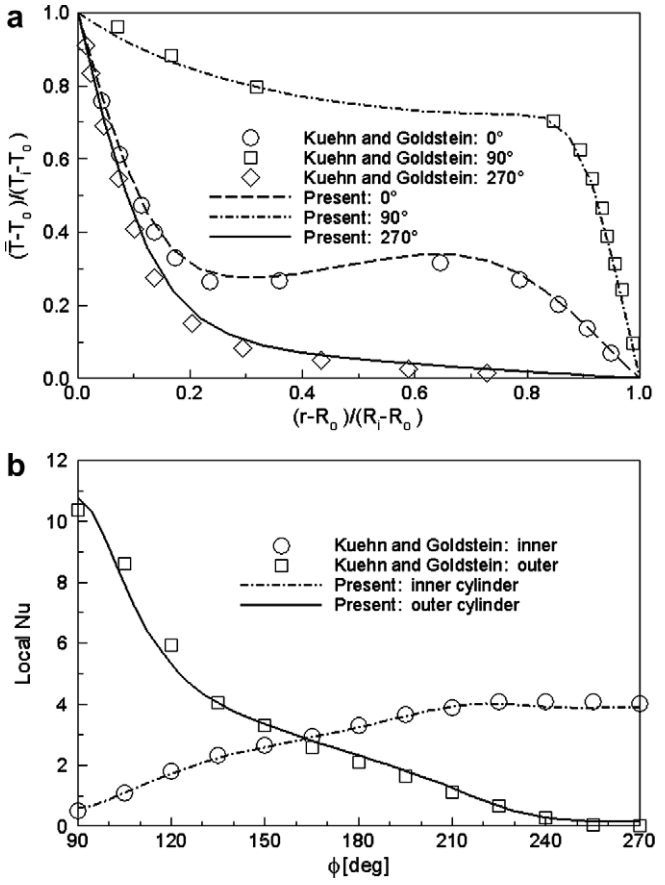

Fig. 2. Comparison with experimental data for $Ra = 4.7 \times 10^4$ and $\eta = 2.6$: (a) radial temperature profiles and (b) local Nusselt number.

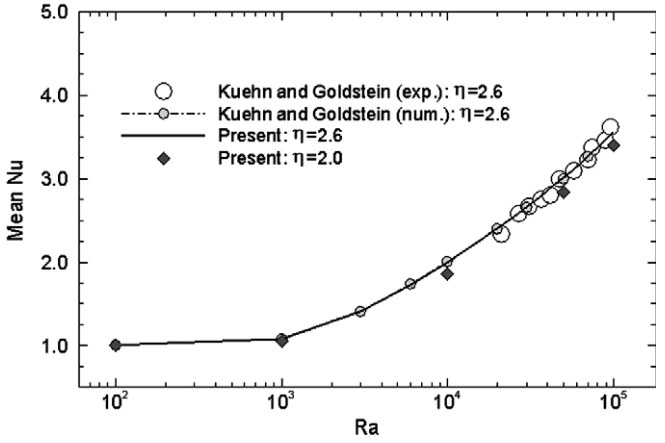

Fig. 3. Mean Nusselt number as function of Rayleigh number for $\eta = 2$ and 2.6; comparison with numerical and experimental results [6].

The Nusselt numbers at the inner and outer cylinders are represented, respectively, by Nu_i and Nu_o. They are given by

$$Nu_i = R_i \ln\left[\frac{R_o}{R_i}\right]\left.\frac{\partial \overline{T}}{\partial r}\right|_{r=R_i}, \quad Nu_o = R_o \ln\left[\frac{R_o}{R_i}\right]\left.\frac{\partial \overline{T}}{\partial r}\right|_{r=R_o}. \quad (21)$$

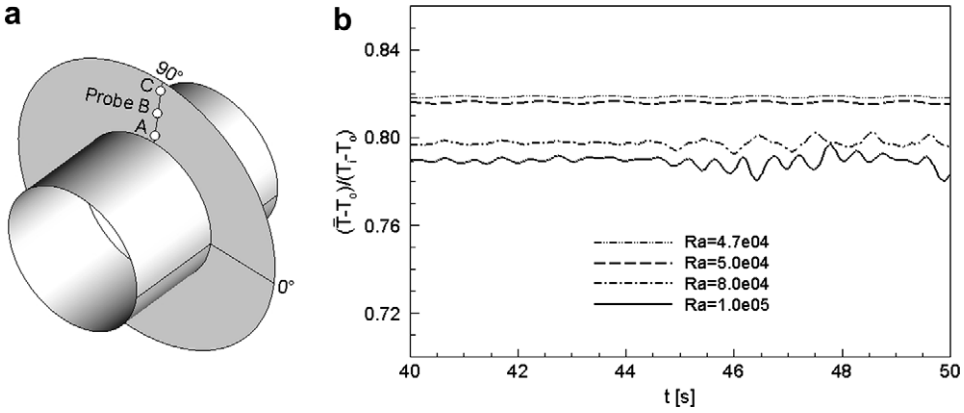

Fig. 4. Probe position and time distribution of the temperature for several *Ra* captured by probe B.

The mean Nusselt number is also defined by

$$\overline{Nu} = \frac{\overline{Nu}_i + \overline{Nu}_o}{2}, \tag{22}$$

where

$$\overline{Nu}_i = \frac{1}{2\pi\lambda}\int_0^{\lambda}\int_0^{2\pi} Nu_i \, d\phi \, dz,$$
$$\overline{Nu}_o = \frac{1}{2\pi\lambda}\int_0^{\lambda}\int_0^{2\pi} Nu_o \, d\phi \, dz. \tag{23}$$

The radial temperature distribution for $\phi = 0°$, 90° and 270° and the local Nusselt numbers Nu_i and Nu_o are presented in Fig. 2. The present work results agree very well with reference results. The average differences between numerical and experimental Nu_i and Nu_o are less than 1.0%.

The mean Nusselt number is presented in Fig. 3 and compared with results of Kuenh and Goldstein [6]. These results present a very good agreement with an average

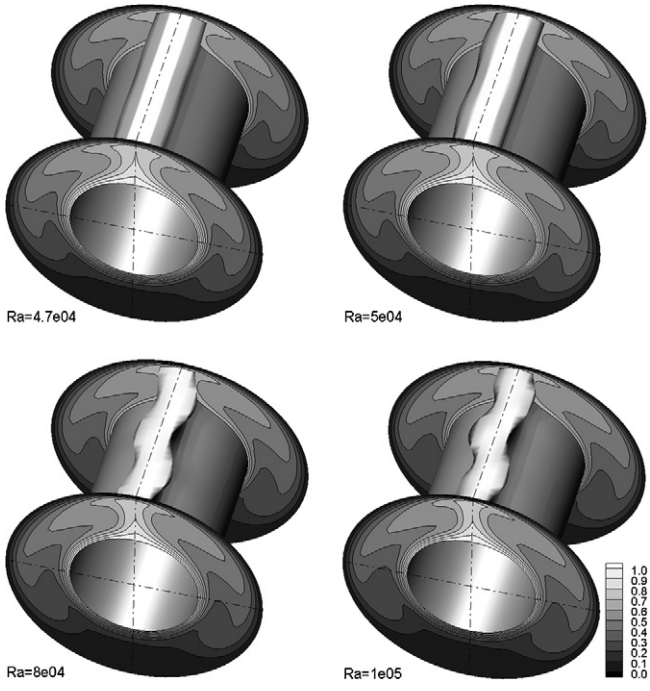

Fig. 5. Instantaneous fields and iso-surfaces of temperature $(\bar{T} - T_o)/(T_i - T_o) = 0.7$ for several *Ra*.

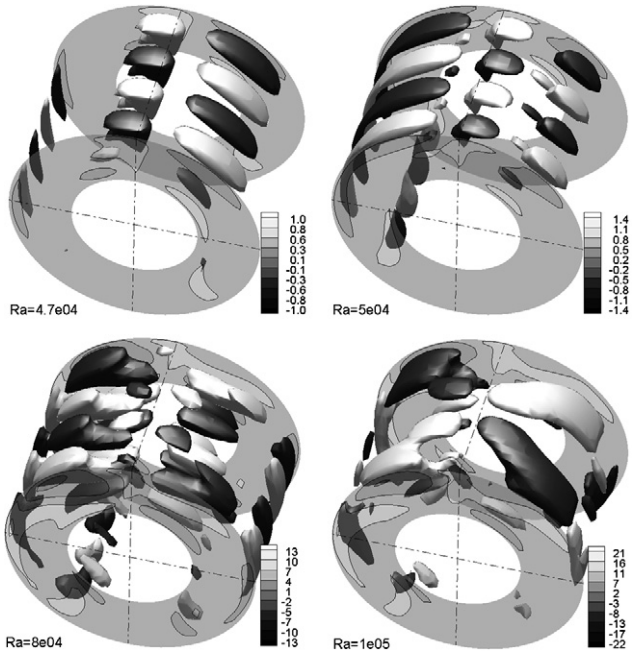

Fig. 6. Instantaneous fields and iso-surfaces of the axial velocity $(\bar{w}L)/v$ for several *Ra*, $\eta = 2$ and $\lambda = 2.8$. Negative iso-surfaces: dark.

Table 1
Maximum values of velocity components for $t = 50$ s

Ra	$\bar{u}L/v$	$\bar{v}L/v$	$\bar{w}L/v$
4.6×10^4	77.04	148.06	0.90
4.7×10^4	78.88	149.83	1.23
4.8×10^4	80.91	149.99	1.65
5×10^4	84.38	153.06	1.74
8×10^4	137.96	215.61	16.05
9×10^4	155.64	223.80	23.50
1×10^5	169.14	249.81	25.85

difference less than 1.53%. In this figure, the geometrical configuration influence on the $\overline{Nu}$ is shown. For low Ra the results are very close. Nevertheless, for higher Ra, where the advection is predominant, the $\overline{Nu}$ for $\eta = 2$ assume values smaller than that for $\eta = 2.6$. This difference is explained by the fact that a small gap inhibits the advective heat transfer process. The local and overall agreement can be regarded as satisfactory, confirming a full credibility of the computational code.

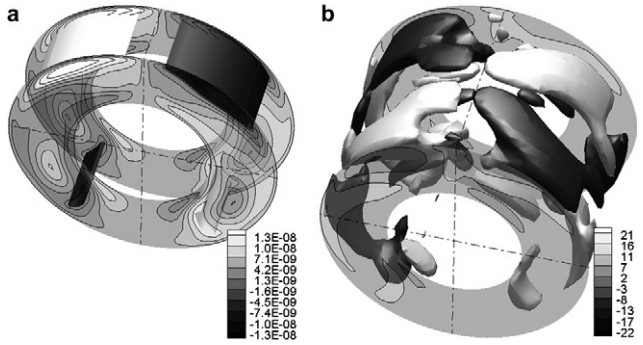

Fig. 7. Instantaneous fields and iso-surfaces of the axial velocity $(\bar{w}L)/v$ for $Ra = 10^5$: (a) $\lambda = 1$ and grid $20 \times 80 \times 2$ and (b) $\lambda = 2.8$ and grid $16 \times 72 \times 24$.

5.2. Unstable flow

Three-dimensional simulations using the dynamic subgrid scale model were performed for $4.6 \times 10^4 \leqslant Ra \leqslant 7.5 \times 10^5$, $\eta = 2$, $\lambda = 2.8$ [24] and a grid of $16 \times 72 \times 24$. The first grid spacing from the walls is $\Delta r = 0.052$ and the maximum $\Delta r = 0.073$. Grid spacing at the other directions are $\Delta\phi = 0.087$ and $\Delta z = 0.116$.

A stable laminar regime exists for Ra up to 4.6×10^4. When the Ra is increased, the flow becomes unstable, as shown in Figs. 4 and 5. In Fig. 4b, temporal temperature distributions were obtained for several Ra at the numerical probe B placed at $r = 1.5$, $\phi = 90°$ and $z = 1.4$, as illustrated by Fig. 4a. The instability onset at the upper part of the cavity presents periodical oscillations with small amplitude, as observed for $Ra = 4.7 \times 10^4$ and 5×10^4 (with fundamental frequencies of 0.7 and 0.74 Hz), in accordance with Powe et al. [44] and Kuenh and Goldstein [7]. Moreover, for $Ra = 8 \times 10^4$ and 10^5 the oscillations are affected by non-linear effects. These instabilities will pro-

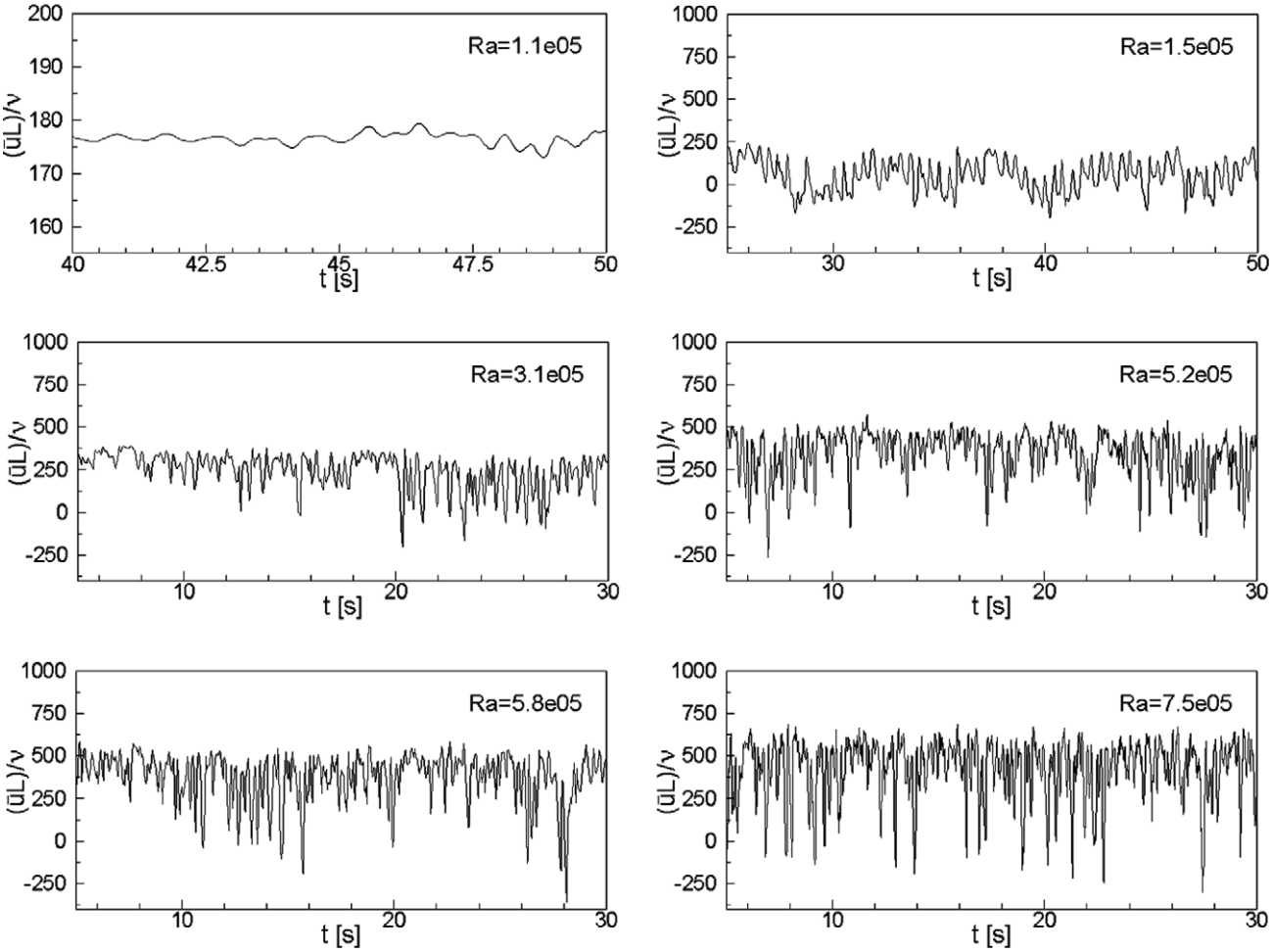

Fig. 8. Time distribution of radial velocity for several Ra at probe B.

mote oscillations of $\overline{Nu}_i$ and $\overline{Nu}_o$ and can be precursors to transition to turbulence.

Fig. 5 shows the effects of instabilities over the thermal plume structure for Ra presented in Fig. 4. In this figure, instantaneous fields (r, ϕ planes) and iso-surfaces (0.7) of dimensionless temperature are visualized. Initially, the thermal plume oscillates axially very slightly. For $Ra \leqslant 8 \times 10^4$ these oscillations display a considerable waving and seem to be moving in all directions. The waves are attenuated as they move downward and can reach $\phi = 0°$ and 180°. As expected, the plume becomes thinner as Ra is increased.

As the flow becomes unstable, the velocity field suffers important changes, i.e., the axial velocity component assumes non-zero values and increases rapidly, as can be seen in Fig. 6 and Table 1. In this figure, the iso-surfaces of instantaneous axial velocity, ±0.5, ±0.7, ±6 and ±10 corresponding, respectively, to $Ra = 4.7 \times 10^4$, 5×10^4, 8×10^4 and 10^5, are plotted. It is interesting to observe that there are two pair of counter-rotating structures (positive: dark) for Ra up to 8×10^4 and that this structures merge to form only one pair for $Ra = 10^5$. The maximum values of velocity components, found at the plume region, are given in Table 1 for several values of Ra. As early mentioned, these values show that the axial velocity becomes important as Ra increases. When compared with the velocity modulus $\sqrt{\bar{u}^2 + \bar{v}^2 + \bar{w}^2}$, axial velocity represents 0.73% and 8.54% for $Ra = 4.7 \times 10^4$ and 10^5, respectively.

Comparison between two-dimensional approximation and three-dimensional results for $Ra = 10^5$ are presented in Fig. 7. In Fig. 7a, symmetric axial velocity fields of insignificant magnitude are observed. The images show that it is impossible numerically to point out the unstable nature of the flow with two-dimensional simulation, not even with three-dimensional simulation that adopts grid of two-dimensional approach.

The results presented show that the onset of unstable flow appears at $Ra \cong 4.7 \times 10^4$. As the Rayleigh number is increased, $Ra \geqslant 10^5$, the oscillatory flow shows irregular non-periodic instabilities.

5.3. Transition to turbulence

Fig. 8 shows the temporal distribution of radial dimensionless velocity for several values of Ra. The sampling was performed using the probe B. The instabilities present amplification in amplitude and frequency as Ra is increased. For $1.1 \times 10^5 \leqslant Ra \leqslant 1.5 \times 10^5$, these instabilities amplify and change dramatically. For $Ra > 1.5 \times 10^5$, a chaotic behavior is observed and a wide band of frequencies appear. These characteristics, more visible for $Ra \geqslant 5.2 \times 10^5$, are typical of turbulent flow. The behavior of the flow is dependent on the observed point in the domain (this is a characteristic of buoyancy-driven flows), i.e., the temperature, for example, present weak fluctuations at the probe A, near inner cylinder, and strong fluctuations at the probe C, near outer cylinder.

The physical mechanisms of transition to turbulence are very dependent on the thermal plume, as visualized in Figs. 9–13. In these figures, instantaneous iso-surfaces of dimensionless temperature (0.25 and 0.5: transparent, 0.65: dark) are presented. Fig. 9 shows, for $Ra = 1.1 \times 10^5$, a thermal plume similar to the plume for $Ra = 1 \times 10^5$ (Fig. 5), but with big amplitude and small wavelength. Increasing Ra to 1.5×10^5 gives rise to strong instabilities in angular direction. Three-dimensional effects are very strong, characterizing the transition to turbulence. When the Rayleigh number is increased to $Ra \geqslant 3.1 \times 10^5$, the plume gradually loses spacial periodicity and an irregular topology appears. As Ra is increased the flow structure becomes very complex and the organized plume structure disappear. For $Ra = 5.8 \times 10^5$ the flow becomes chaotic with turbulent features, presenting advective transport of the heated mass for both side of the cavity.

In Fig. 10, the temporal evolution of two isothermal surfaces are depicted for $Ra = 1.7 \times 10^5$ at different times:

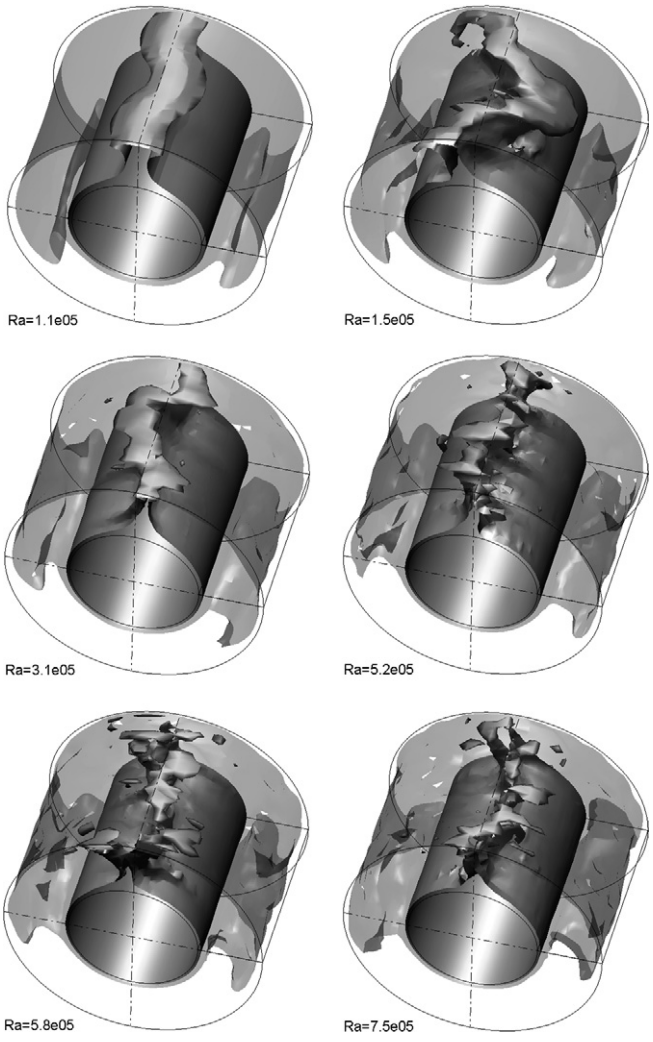

Fig. 9. Instantaneous temperature iso-surfaces $(\overline{T} - T_o)/(T_i - T_o)$ for several Ra: 0.25 (transparent) and 0.65 (dark).

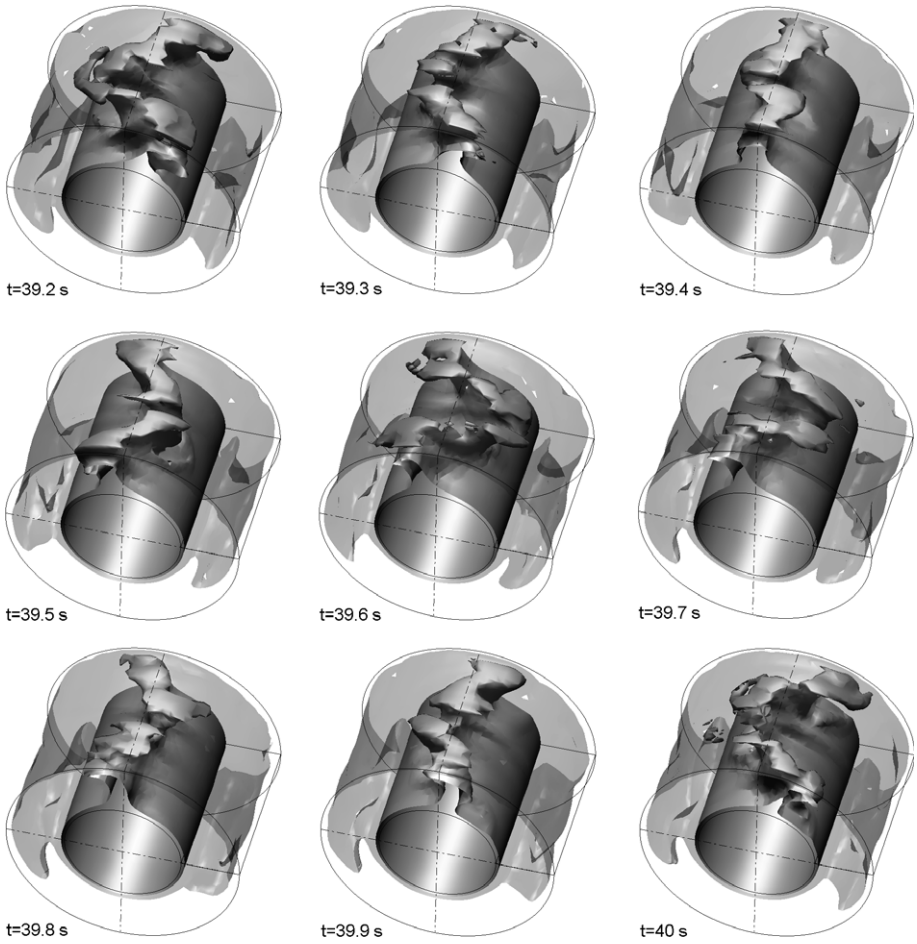

Fig. 10. Temporal evolution of the temperature iso-surfaces $(\overline{T} - T_o)/(T_i - T_o)$ for $Ra = 1.7 \times 10^5$: 0.25 (transparent) and 0.65 (dark).

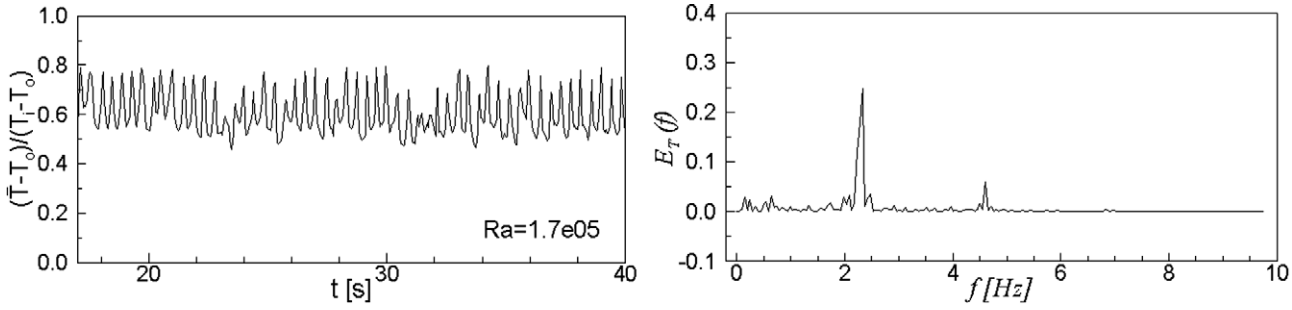

Fig. 11. Time distribution of temperature (probe B) and power spectra of temperature fluctuations for $Ra = 1.7 \times 10^5$.

39.2–40 s. The three-dimensional effects are very strong and one can observe that the plume oscillates with vigorous amplitude, moving from left to right and back, as observed experimentally in [8,45]. Considering the position of the center of the plume, one can see that it passes by $\phi = 90°$ at $t \cong 39.4$ s and at $t \cong 39.8$ s, when the plume complete one temporal cycle. Approximately, it gives a fundamental frequency of 2.5 Hz. In order to determine more precisely this frequency, the Fourier Transform of the time distribution of temperature at probe B is shown in Fig. 11. It is found that the fundamental frequency is approximately 2.33 Hz. We see that the fundamental frequency determined by the visualization is close to that frequency determined by the statistical procedure.

Another temporal series (29.2–30 s) of three isothermal surfaces for $Ra = 5.8 \times 10^5$ (Fig. 12), shows chaotic features. The lower frequencies are controlled by the gap of the cavity, and the higher frequencies are controlled by Ra. Certainly, all these frequencies cannot be visualized using the isothermal surfaces. Alternatively, the vortical structures associated with irregular thermal structures are given in Fig. 13, using streamlines projected at three planes

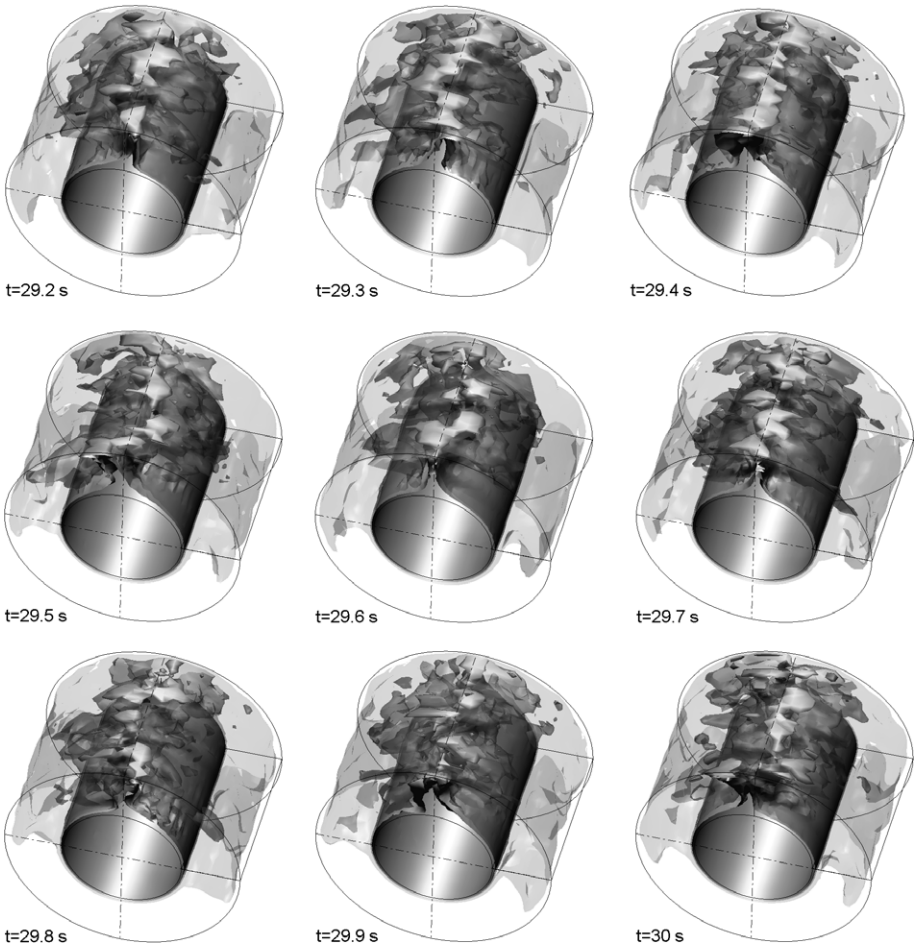

Fig. 12. Temporal evolution of temperature iso-surfaces $(\overline{T}-T_o)/(T_i-T_o)$ for $Ra = 5.8 \times 10^5$: 0.25, 0.5 (transparent) and 0.65 (dark).

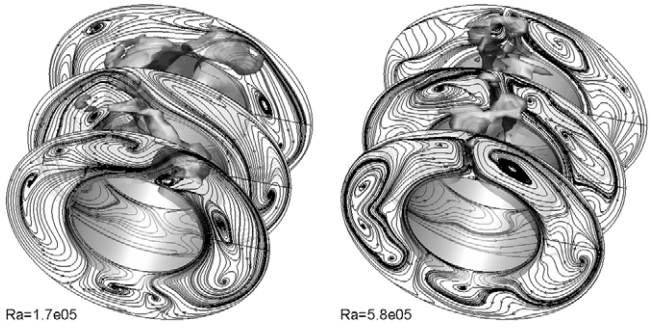

Fig. 13. Instantaneous streamlines combined with iso-surfaces of temperature $(\overline{T}-T_o)/(T_i-T_o) = 0.65$ for two values of Ra.

(r,ϕ). At the upper part of the annulus the flow is very unstable and the intensity of turbulence is high. At the lower part of the annulus, the flow is still unstable, but the intensity of turbulence is smaller.

Numerical results of the present work are in agreement with experimental observations of Powe et al. [44], Bishop et al. [45], Kuehn and Goldstein [7], Labonia and Guj [9] and with the sketch about the structure of the flow, present by McLeod and Bishop [8]. It is important to empathize that, as shown in Fig. 13, even in the lower part of the cavity the flow is unstable.

The authors of the present work believe that the results presented here can elucidate better the physical behavior of the flow in the entire domain, which is very unstable.

5.3.1. Energy spectrum

The Kolmogorov theory [46] for developed turbulence determines that the inertial band of the spectra presents a $-5/3$ law. This theory gives rise to the famous Kolmogorov law [27]. In the present work, this law was used in order to verify if the simulated flows attain the turbulent regime.

The energy spectrum of the radial velocity fluctuation (probe B) for several Ra are presented in Fig. 14. First, it can be observed that the energy of the large structures increases for higher values of Ra. For $Ra = 1.5 \times 10^5$ the spectral energy is almost concentrated at the bigger structures, showing an inertial slope greater than $-5/3$. For higher Ra the energy is better distributed over all the spectrum of turbulent structures, giving a slope nearest to $-5/3$, in accordance with the Kolmogorov law. For instance, the energy spectrum for $Ra = 5.8 \times 10^5$ and 7.5×10^5 present a

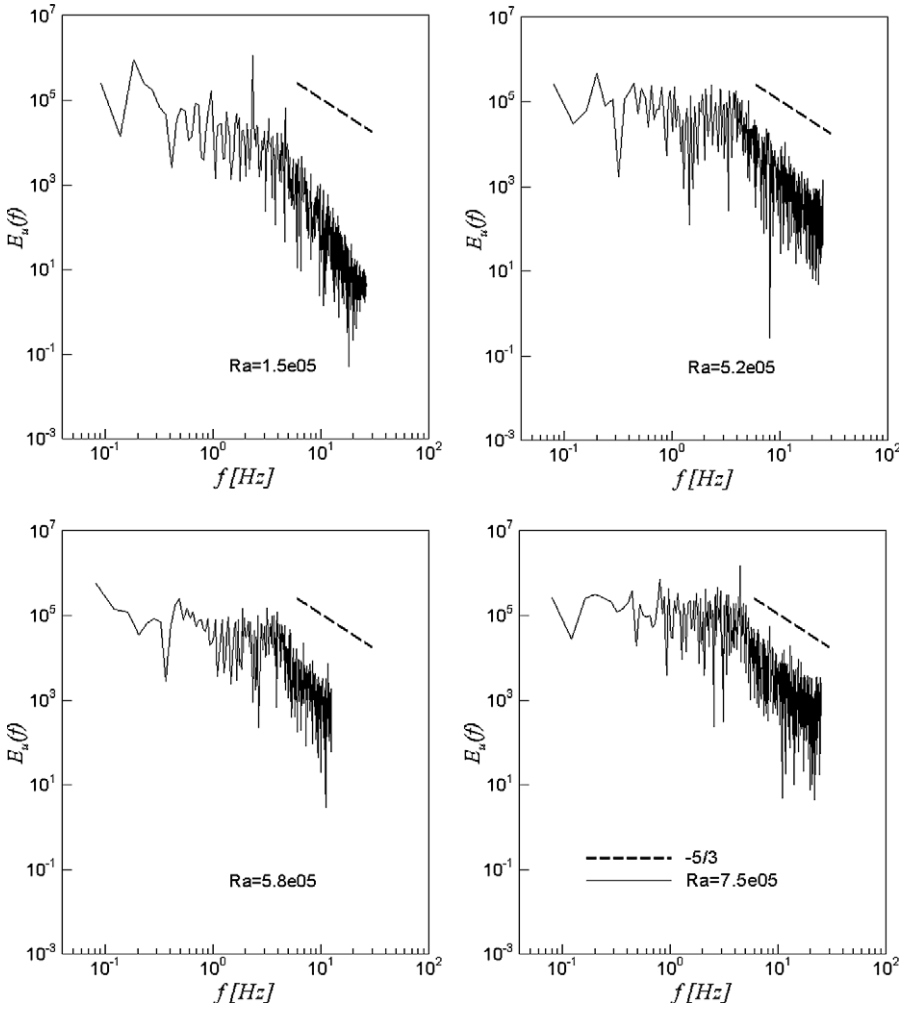

Fig. 14. Energy spectra of the radial velocity component fluctuation for several Ra.

good approximation of $-5/3$. Also, one observes that the inertial range increases with Ra.

The energy spectrum for $Ra = 1.5 \times 10^5$ suggests an important contribution from the small structures. It is confirmed from the turbulent eddy viscosity field, where maximum value is 0.84ν. As an additional commentary, the maximum ν_t obtained for $Ra = 10^5$ and 1.1×10^5 are 0.05ν and 0.15ν.

5.3.2. Comparison with experimental data

Statistical results are compared with experimental results [24] and with the correlation of Itoh et al. [10]. Fukuda et al. [24] used an experimental device with $\eta = 2$ and $\lambda = 3.55$ and hot-wire anemometry. Itoh et al. [10] used the characteristic length defined as $l_m = \ln(R_o/R_i)\sqrt{R_o R_i}$ and experimental results [4,1] in order to determine an expression for $\overline{Nu}$, which is given by

$$\overline{Nu} = 0.18\frac{(Ra_m)^{1/4}}{Pr}, \quad (Pr = 0.71,\ Ra_m \geqslant 7.1 \times 10^3), \tag{24}$$

where Ra_m is the Rayleigh number based on l_m. Eq. (22) is still valid for unstable flow, but redefining this expression to calculate Nu_i and Nu_o (Eq. 23), the following expressions are now used:

$$\overline{Nu_i} = \frac{1}{2\pi\lambda(t_2 - t_1)}\int_{t_1}^{t_2}\int_0^{\lambda}\int_0^{2\pi} Nu_i \,d\phi\, dz\, dt, \tag{25}$$

$$\overline{Nu_o} = \frac{1}{2\pi\lambda(t_2 - t_1)}\int_{t_1}^{t_2}\int_0^{\lambda}\int_0^{2\pi} Nu_o \,d\phi\, dz\, dt, \tag{26}$$

where $(t_2 - t_1)$ represents the time to obtain statistical samples.

Fig. 15 shows the radial distribution of the mean dimensionless temperature at $\phi = 90°$ and $345°$ and $z = 1.4$, for four values of Ra. The temperature distribution at $\phi = 90°$ decreases as Ra increases, as a consequence of the diffusion of energy in angular direction. The agreement between these results and experiment is very good, except for $Ra = 1.1 \times 10^5$ and 1.7×10^5 at $\phi = 90°$. These differences observed for $\phi = 90°$ can be due to experimental

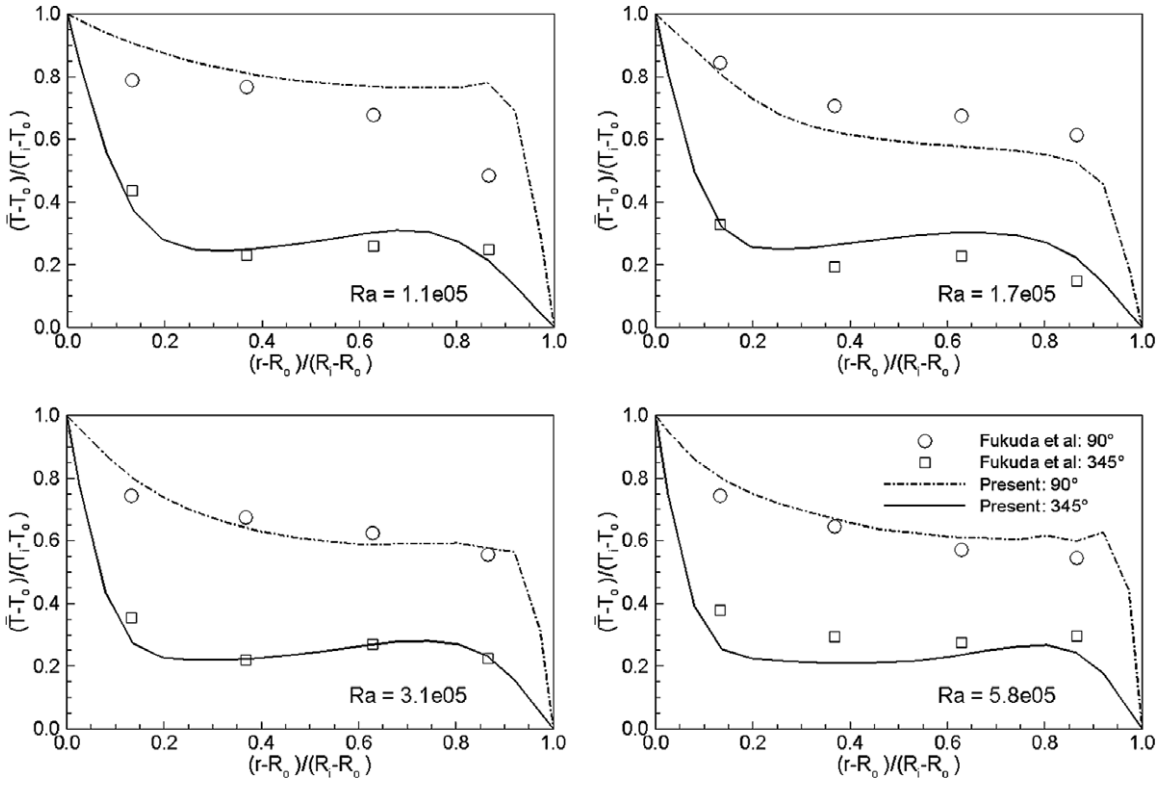

Fig. 15. Comparison with experimental time-averaged temperature distributions for several *Ra*.

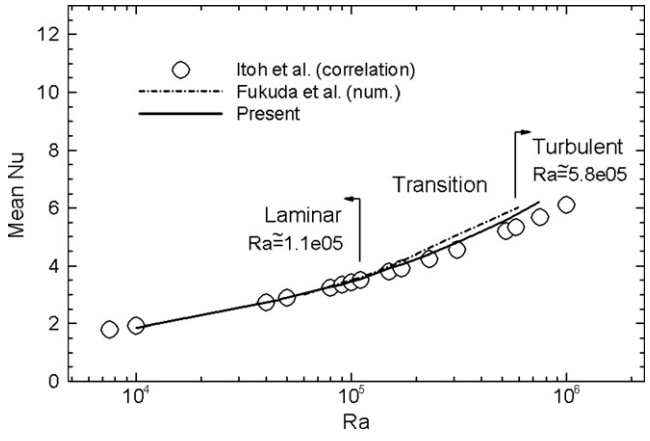

Fig. 16. Mean Nusselt number as function of Rayleigh number for $\eta = 2$ and $\lambda = 2.8$.

error [24], which is assumed to be 30% (maximum) for flows at low velocities.

The agreement of the Nusselt number with results of Itoh et al. [10] and Fukuda et al. [24] is satisfactory, as can be visualized in Fig. 16. In this figure, transition to turbulence is suggested corresponding to $1.1 \times 10^5 < Ra \leqslant 5.8 \times 10^5$. It was determined using physical analysis presented in the previous Sections 5.2 and 5.3. In transition and turbulent regimes there is a difference between the results of the present work and that of Itoh et al. [10] and Fukuda et al. [24]. The average of those differences are 3.09% and 2.93%, respectively. It seems that numerical results of Fukuda et al. [24] give instabilities that are over predicted. On the other hand, the results show that transition to turbulence and turbulence accelerate the heat transfer process.

The heat balance between the inner and outer cylinders surfaces is very good, as shown at Table 2, where the relative difference between $\overline{Nu}_i$ and $\overline{Nu}_o$ is smaller than 1% for all cases considered. This table also shows the average time step used.

Table 2
Mean Nusselt number at inner and outer cylinder surfaces, $\eta = 2$, $\lambda = 2.8$ and grid $16 \times 72 \times 24$

Ra	d*t* (s)	$\overline{Nu}_i$	$\overline{Nu}_o$	Error (%)
4.6×10^4	1.47×10^{-3}	2.826	2.826	0.00
4.7×10^4	1.47×10^{-3}	2.842	2.842	0.00
4.8×10^4	1.47×10^{-3}	2.858	2.858	0.00
5.0×10^4	1.46×10^{-3}	2.888	2.888	0.00
8.0×10^4	1.39×10^{-3}	3.259	3.261	0.06
9.0×10^4	1.38×10^{-3}	3.359	3.360	0.03
1.0×10^5	1.36×10^{-3}	3.450	3.449	0.03
1.1×10^5	1.39×10^{-3}	3.533	3.532	0.03
1.5×10^5	1.20×10^{-3}	3.926	3.898	0.71
1.7×10^5	1.04×10^{-3}	4.064	4.043	0.52
2.3×10^5	1.09×10^{-3}	4.407	4.386	0.48
3.1×10^5	9.76×10^{-4}	4.802	4.778	0.50
5.2×10^5	7.78×10^{-4}	5.596	5.554	0.75
5.8×10^5	7.80×10^{-4}	5.774	5.728	0.80
7.5×10^5	7.09×10^{-4}	6.250	6.196	0.86

6. Conclusions

Numerical simulations of natural convection inside an annular cavity, composed by two horizontal concentric cylinders, were performed using large-eddy simulation methodology with dynamic sub-grid scale model. Unstable flows were simulated and analyzed, considering the parameter $\eta = 2$ and $\lambda = 2.8$ and several Rayleigh numbers. It is well know that LES is not applicable to simulate transition to turbulence. This is a conceptual point of view. Nevertheless, this methodology was applied in the present work and the physical and overall results seem to demonstrate that LES can be used to predict transition to turbulence problems.

The two-dimensional simulations cannot provide any physical instabilities, up to $Ra = 10^5$, as expected. The three-dimensional simulations pointed out the first typical instabilities of the transition process at the upper part of the cavity. As the Rayleigh number increases, the flow initially periodic, becomes unstable and irregular and the instabilities reach the lower part of the cavity. In turbulent regime, the flow shows strong and chaotic instabilities, where a large band of frequencies are present.

The dynamic characteristics of the flow, as well as physical aspects of the thermal plume transition were well captured. Turbulent structures were found in all the interior of the cavity. Nevertheless, at the lower part of the cavity these structures posses smaller turbulence intensity. The *Ra* values for the onset of the first instabilities and onset of transition to turbulence and turbulent regime were suggested.

The influence of the instabilities on the heat transfer was quantified. With increasing of *Ra*, the slope of the mean Nusselt number changes approximately for $Ra \geqslant 1.5 \times 10^5$.

Acknowledgements

The authors would like to thank the Brazilian Council of Research and Development (CNPq) for the financial support and to the School of Mechanical Engineering of the Federal University of Uberlândia.

References

[1] W. Beckmann, Die Wärmeübertragung in zylindrischen gasschichten bei natürlicher konvektion, Forsh. auf dem Geb. des Ing. 2 (4) (1931) 165–178.
[2] H. Voig, O. Krischer, Die wärmeübertragung in zylindrischen luftschichten bei natürlicher konvektion, Forsh. Grn. D. Ing. 3 (6) (1932) 303–306.
[3] H. Kraussold, Wärmeabgabe von zylindrischen flüssigkeitschichten bei natürlicher konvektion, Forsch. auf dem Geb. des Ing. Bd. 5 (4) (1934) 189–191.
[4] U. Grigull, W. Hauf, Natural convection in horizontal cylindrical annuli, in: Proceedings of the Third International Heat Transfer Conference, Chicago, 1966, pp. 182–195.
[5] E.H. Bishop, C.T. Carley, Photographic studies of natural convection between concentric cylinders, Heat Transfer Fluid Mech. Inst. (1966) 63–78.
[6] T.H. Kuehn, R.J. Goldstein, An experimental and theoretical study of natural convection in the annulus between horizontal concentric cylinders, J. Fluid Mech. 74 (4) (1976) 695–720.
[7] T.H. Kuehn, R.J. Goldstein, An experimental study of natural convection heat transfer concentric and eccentric horizontal cylindrical annuli, J. Heat Transfer 100 (1978) 635–640.
[8] A.E. McLeod, E.H. Bishop, Turbulent natural convection of gases in horizontal cylindrical annuli at cryogenic temperatures, Int. J. Heat Mass Transfer 32 (10) (1989) 1967–1978.
[9] G. Labonia, G. Guj, Natural convection in a horizontal concentric cylindrical annulus: oscillatory flow and transition to caos, Int. J. Fluid Mech. 375 (1998) 179–202.
[10] M. Itoh, T. Fujita, N. Nishiwaki, M. Hirata, A new method of correlating heat-transfer coefficients for natural convection in horizontal cylindrical annuli, Int. J. Heat Mass Transfer 13 (1970) 1364–1369.
[11] L. Crawford, R. Lemlich, Natural convection in horizontal concentric cylindrical annuli, I. E. C. Fund. 1 (1962) 260–264.
[12] S. Shibayama, Y. Mashimo, Natural convection heat transfer in horizontal concentric cylindrical annuli, Papers J. S. M. E. Nat. Symp., vol. 169, 1963, pp. 7–20.
[13] R.E. Powe, C.T. Carley, S.L. Carruth, A numerical solution for natural convection in cylindrical annuli, J. Heat Transfer 92 (12) (1971) 210–220.
[14] T.H. Kuehn, R.J. Goldstein, An experimental study of natural convection heat transfer in concentric and eccentric horizontal cylindrical annuli, ASME J. Heat Transfer 100 (1976) 640–653.
[15] E. Van de Sande, B.J.G. Hamer, Steady and natural convection in enclosures between horizontal circular cylinders (constant heat flux), Int. J. Heat Mass Transfer 22 (1979) 361–370.
[16] Y.T. Tsui, B. Tremblay, On transient natural convection heat transfer in the annulus between concentric horizontal cylinders with isothermal surfaces, Int. J. Heat Mass Transfer 27 (1) (1984) 103–111.
[17] B. Farouk, S.I. Guçeri, Laminar and turbulent natural convection in the annulus between horizontal concentric cylinders, J. Heat Transfer 104 (1982) 631–636.
[18] M.I. Char, Y.H. Hsu, Comparative analysis of linear and nonlinear low-Reynolds-number eddy viscosity models to turbulent natural convection in horizontal cilyndrical annuli, Numer. Heat Transfer A 33 (1986) 191–206.
[19] S. Kenjeres, K. Hanjalic, Prediction of turbulent thermal convection in concentric and exccentric horizontal annuli, Int. J. Heat Fluid Flow 16 (5) (1995) 429–439.
[20] T. Fusegi, B. Farouk, A tree-dimensional study of natural convection in the annulus between, horizontal concentric cylinder, in: Proceedings of the Eighth International Heat Transfer Conference, vol. 4, 1986, pp. 1575–1580.
[21] K. Vafai, J. Ettefagh, An investigation of transient tree-dimensional buoyancy-driven flow and heat transfer in a closed horizontal annulus, Int. J. Heat Mass Transfer 34 (10) (1991) 2555–2570.
[22] K. Vafai, J. Ettefagh, Comparative analysis of the finite-element and finite-difference methods for simulation of buoyancy-induced flow and heat transfer in closed and open ended annular cavities, Numer. Heat Transfer 23A (1993) 35–59.
[23] C.P. Desai, K. Vafai, An investigation and comparative analysis of two-and tree-dimensional turbulent natural convection in a horizontal annulus, Int. J. Heat Mass Transfer 37 (16) (1994) 2475–2504.
[24] K. Fukuda, Y. Miki, S. Hasegawa, Analytical and experimental study on turbulent natural convection in a horizontal annulus, Int. J. Heat Mass Transfer 33 (4) (1990) 629–639.
[25] Y. Miki, K. Fukuda, N. Taniguchi, Large eddy simulation of turbulent natural convection in concentric horizontal annuli, Int. J. Heat Fluid Flow 14 (3) (1993) 210–216.
[26] J. Smagorinsky, General circulation experiments with the primitive equations, Mon. Weather Rev. 91 (1963) 99–115.
[27] M. Lesieur, Turbulence in Fluids, Kluwer Academic, 1997.
[28] M. Germano, A proposal for a definition of the turbulent stresses in filtred Navier–Stokes equations, Phys. Fluid 29 (7) (1996) 2323–2324.
[29] T.M. Eidson, Numerical simulation of the turbulent Rayleigh–Benard problem using subgrid modeling, J. Fluid Mech. 158 (1985) 245–268.

[30] A. Yoshizawa, A statistical theory of themally-driven turbulent shear flows with the derivation of a subgrid model, J. Phys. Soc. J. 52 (1983) 1194–1205.
[31] A. Silveira-Neto, D. Grand, O. Metais, M. Lesieur, A numerical investigation of the coherent structures of turbulence behind a backward-facing step, J. Fluid Mech. 256 (1993) 1–25.
[32] M. Germano, U. Piomelli, P. Moin, W.H. Cabot, A dynamic subgrid-scale eddy viscosity model, Phys. Fluid A 3 (7) (1991) 1760–1765.
[33] D.K. Lilly, A proposed modification of the Germano subgrid-scale closure method, Phys. Fluid A 4 (3) (1992) 633–635.
[34] U. Piomelli, B.H. Cabot, P. Moin, S. Lee, Subgrid-scale backscatter in turbulent and transitional flows, J. Phys. Fluid A 3 (1991) 1766–1771.
[35] J.H. Ferziger, M. Peric, Computational Methods for Fluid Dynamics, Springer, 1999.
[36] E.L.M. Padilla, Large-eddy simulation of transition to turbulence in rotating system with heat transfer, Doctor Thesis, Federal University of Uberlândia, Uberlândia, MG, 2004.
[37] E.L.M. Padilla, A. Silveira-Neto, Large-eddy simulation of transition to turbulence in a heated annular channel, C. R. Mecanique 333 (2005) 599–604.
[38] S.V. Patankar, Numerical Heat Transfer and Fluid Flow, McGraw-Hill, 1980.
[39] C.R. Maliska, Transferência de calor e mecânica dos fluidos computacional, Livros Técnicos e Científicos Editora, 1995.
[40] J. Kim, P. Moin, Application of a fractional step method to incompressible Navier–Stokes equations, J. Comp. Phys. 59 (1985) 308–323.
[41] H.L. Stone, Iterative solution of implicit approximations of multidimensional partial differential equations, SIAM J. Numer. Anal. 5 (1968) 530–558.
[42] U. Piomelli, A. Scotti, E. Balaras, Large-eddy simulation of turbulent flows from desktop to supercomputer, Proceeding of the Fourth International Conference on Vector and Parallel Processing, vol. 3, Springer, 2000.
[43] M. Villand, Trio-VF Technics relatory-note de presentation de la version octobre 86, Centre D'Etudes Nucleaires de Grenoble, France, 1986.
[44] R.E. Powe, C.T. Carley, C.T. Bishop, Free convective flow patterns in cylindrical annuli, J. Heat Transfer 91 (1969) 310–314.
[45] E.H. Bishop, C.T. Carley, R.E. Powe, Natural convective oscillatory flow in cylindrical annuli, Int. J. Heat Mass Transfer 11 (1968) 1741–1752.
[46] A.N. Kolmogorov, On generation (decay) of isotropic turbulence in an incompressible viscous liquid, Dokl. Akad. Nauk. SSSR 31 (1941) 538–540.